



Original paper

Design and development of a dedicated portable gamma camera system for intra-operative imaging



Sanaz Kaviani^a, Navid Zeraatkar^a, Salar Sajedi^a, Afshin Akbarzadeh^a, Nahid Gorjizadeh^{a,b}, Mohammad Hossein Farahani^a, Behnoosh Teimourian^a, Pardis Ghafarian^{c,d}, Hamid Sabet^e, Mohammad Reza Ay^{a,b,*}

^a Research Center for Molecular and Cellular Imaging, Tehran University of Medical Sciences, Tehran, Iran

^b Department of Medical Physics and Biomedical Engineering, Tehran University of Medical Sciences, Tehran, Iran

^c Chronic Respiratory Disease Research Center, NRITLD, Masih Daneshvari Hospital, Shahid Beheshti University of Medical Sciences, Tehran, Iran

^d PET/CT and Cyclotron Center, Masih Daneshvari Hospital, Shahid Beheshti University of Medical Sciences, Tehran, Iran

^e Massachusetts General Hospital, Harvard Medical School, Boston, USA

ARTICLE INFO

Article history:

Received 27 February 2016

Received in Revised form 14 May 2016

Accepted 10 June 2016

Available online 23 June 2016

Keywords:

Sentinel lymph node (SLN)

Lymphoscintigraphy

SURGEOSIGHT-I

Breast cancer

Intra-operative gamma camera

ABSTRACT

Purpose: We developed a high performance portable gamma camera platform dedicated to identification of sentinel lymph nodes (SLNs) and radio-guided surgery for cancer patients. In this work, we present the performance characteristics of SURGEOSIGHT-I, the first version of this platform that can intra-operatively provide high-resolution images of the surveyed areas.

Methods: At the heart of this camera, there is a 43×43 array of pixelated sodium-activated cesium iodide (CsI(Na)) scintillation crystal with $1 \times 1 \text{ mm}^2$ pixel size and 5 mm thickness coupled to a Hamamatsu H8500 flat-panel multi-anode (64 channels) photomultiplier tube. The probe is equipped with a hexagonal parallel-hole lead collimator with 1.2 mm holes. The detector, collimator, and the associated front-end electronics are encapsulated in a common housing referred to as head.

Results: Our results show a count rate of ~ 41 kcps for 20% count loss. The extrinsic energy resolution was measured as 20.6% at 140 keV. The spatial resolution and the sensitivity of the system on the collimator surface was measured as 2.2 mm and 142 cps/MBq, respectively. In addition, the integral and differential uniformity, after uniformity correction, in useful field-of-view (UFOV) were measured 4.5% and 4.6%, respectively.

Conclusions: This system can be used for a number of clinical applications including SLN biopsy and radiopharmaceutical-guided surgery.

© 2016 Associazione Italiana di Fisica Medica. Published by Elsevier Ltd. All rights reserved.

1. Introduction

A key prognostic factor in patients with early stage cancer is the metastases status of the regional nodes draining the primary tumor [1–3]. The metastasis to local and distant nodes helps identifying the choice of therapy, tumor staging, and patient's outcome. Sentinel lymph node (SLN) concept and lymphatic mapping [4,5] is considered the current standard of care in which the cancer patient is injected with either blue dye (followed by direct vision during surgery) or radiopharmaceuticals for scintigraphic mapping with a gamma camera and intraoperative identification of sentinel

lymph nodes (using a gamma probe). The SLN is defined as the first node of lymphatic drainage from the primary tumor [6,7].

While conventional gamma cameras are still used for pre-operative lymphoscintigraphy, their geometry and performance are not optimized for detecting lymph nodes. The use of portable gamma cameras and intra-operative probes is justified by the close proximity of the detector to a tumor or node during surgery which leads to increased solid angle and enhances the detection efficiency.

In recent years, portable gamma camera systems have received much attention to perform SLN lymphoscintigraphy [8]. The main applications of such dedicated small-sized intra-operative imaging systems are the detection of SLNs in breast cancer and melanoma, and functional imaging of the thyroid and parathyroid glands [9,10].

Recently, several portable gamma camera designs have been proposed for SLN surgery in breast cancer patients [9,11–15].

* Corresponding author at: Department of Medical Physics and Biomedical Engineering, Tehran University of Medical Sciences, Tehran, Iran.

E-mail address: mohammadreza_ay@tums.ac.ir (M.R. Ay).

Trotta et al. [16] developed a gamma camera consisting of a pixelated CsI(Na) crystal array with 2.45 mm pixel pitch coupled to a position-sensitive photomultiplier tube (PSPMT) and a parallel-hole collimator for intra-operative imaging. They achieved a spatial resolution of 2.5 mm full-width at half-maximum (FWHM) and 204 cps/MBq sensitivity. Olcott et al. [13] constructed a portable gamma camera system based on H8500 square PSPMT coupled to an NaI(Tl) crystal array. The detector was equipped with a high-sensitivity parallel-hole collimator with 1.3 mm hole size, 0.2 mm septa thickness, and 2 cm collimator thickness. The system has a spatial resolution of 1.6 mm (FWHM at 1 cm), sensitivity of 135 cps/MBq, and energy resolution of 12.3%. Fernández et al. [17] designed and developed a mini gamma camera based on a continuous CsI(Na) crystal block with dimension of $50 \times 50 \times 4.6 \text{ mm}^3$, H8500 PSPMT readout, and 2 mm single-pinhole collimator. The characterization of the system was reported as 1.3 mm intrinsic spatial resolution (camera without collimator), 13% energy resolution at 140 keV, and 54 cps/MBq planar sensitivity for the 2 mm pinhole collimator at 4 cm [18]. Knoll et al. [19] reported the characterization of a hand-held gamma camera based on semiconductor with a cadmium-zinc-telluride (CZT). A parallel-square-hole collimator with $2.16 \times 2.16 \text{ mm}$ hole size and 0.3 mm septa was attached to the detector. This system has an intrinsic energy resolution of 5.2%, an integral and differential uniformity of 5.8% and 3.8%, respectively, and a system sensitivity of 237 cps/MBq with low-energy high-resolution (LEHR) collimator.

The aim of this study is to report the design and performance characterization of SURGEOSIGHT-I, a portable gamma camera system that we recently developed at the Research Center for Molecular and Cellular Imaging, Tehran University of Medical Sciences. The performance parameters of the SURGEOSIGHT-I were evaluated according to the NEMA NU1-2007 standard [20].

2. Material and methods

2.1. Camera design

2.1.1. Detection system

The SURGEOSIGHT-I (Fig. 1(a)) detector module consists of a 43×43 array of CsI(Na) scintillator (Hilger Crystals, UK) with pixel dimensions of $1 \text{ mm} \times 1 \text{ mm} \times 5 \text{ mm}$ (1.2 mm pixel pitch) optically glued to a H8500C PSPMT (Hamamatsu Photonic Co., Japan) with $49 \times 49 \text{ mm}^2$ active area. A low-energy general-purpose parallel-hole lead collimator with 1.2 mm hexagonal holes, 18 mm thickness, 0.2 mm septal thickness, and total dimension of $50 \times 50 \text{ mm}^2$ was attached to the front side of the crystal. The detection system including crystal, PSPMT, and electronic boards are placed in housing, shielded by at least 3 mm lead (Fig. 1(b)).

2.1.2. Electronic readout

Dedicated electronics were designed and developed for data acquisition and processing that were placed inside the head or trolley. The trolley is equipped with an adjustable arm (4 degrees of freedom) to provide the required motions around the patient, conveniently (Fig. 1(a)). The readout system consists of one high-voltage (HV) board, a resistive network board, and two amplifier boards which are placed inside the camera head (Fig. 1(b)). Data acquisition board is placed inside the trolley. Moreover, an all-in-one computer is mounted on the trolley for further signal processing, data calibrations, image generation, and displaying the images of the surveyed area. The HV board generates regulated -900 V as bias voltage of the PSPMT. The gain uniformity in 64 channels of PSPMT at this bias voltage is shown in Fig. 2. Relative differences between areas of maximum and minimum pulse height values are 39%.

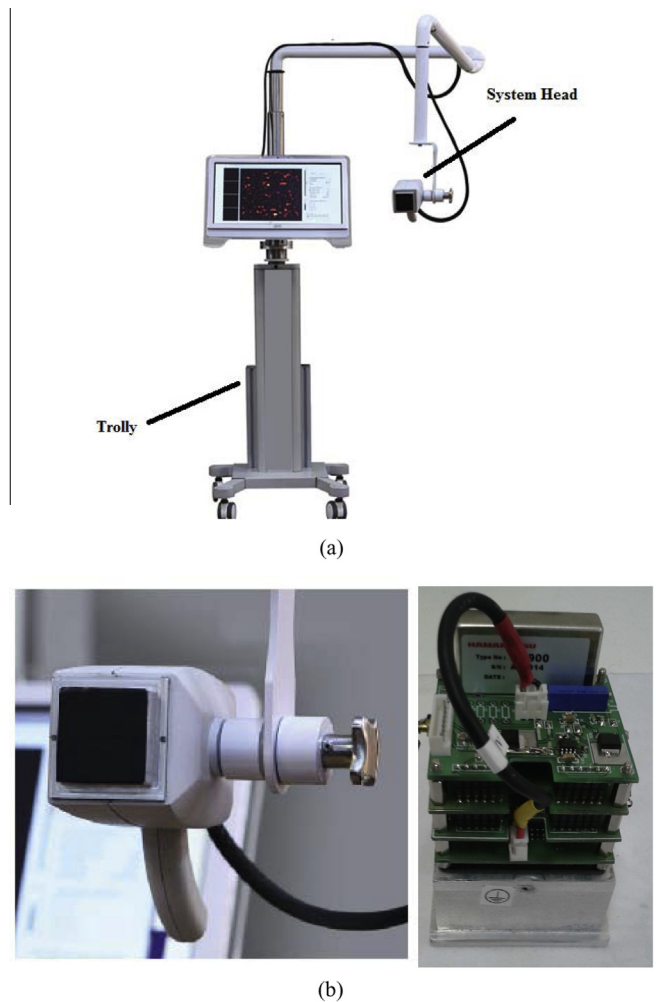


Fig. 1. The SURGEOSIGHT-I system (a), and the system head and front-end electronics (b).

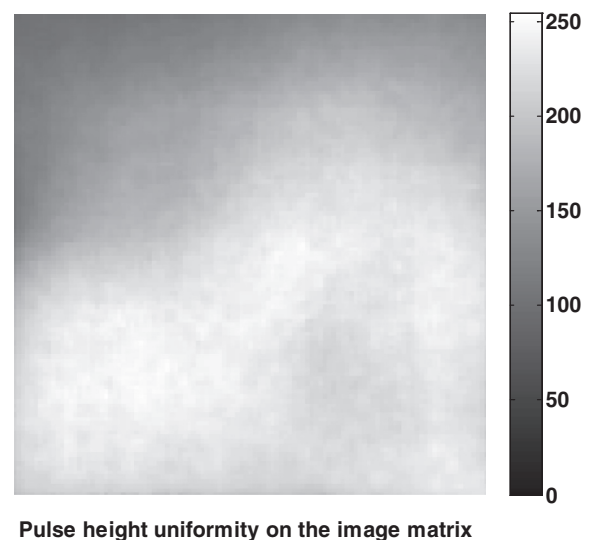


Fig. 2. Image of pulse height uniformity in -900 V as bias voltage. Relative differences between areas of maximum and minimum pulse height values are 39%.

The PSPMT produces 8×8 anode signals which are then summed in rows and columns using a simple resistive network (shown in Fig. 3(a)) to reduce the number of electronic channels.

Pre-amplification of signals is performed with two 8-channel pre-amplification boards identical for X and Y signals (Fig. 3(b) and (c)). After pre-amplification, signals lower than a threshold value are suppressed using a voltage clamping technique in order to increase final positioning accuracy. Acquisition board (Fig. 3(d)) receives four positioning signals from weighted summation of 16 position signals (X_1 – X_8 and Y_1 – Y_8) based on Anger logic event positioning [21]. At the first stage of acquisition process, signals are digitized with four high-speed analog-to-digital converters (ADCs) with 25 MSamples/s sampling rate to obtain the full bandwidth of signals. Energy of the pulses in each channel (X^+ , X^- , Y^+ and Y^-) was also extracted by Anger logic algorithm [21]. Eventually, the digital position values of the incident photon are transferred via Local Area Network (LAN) cable to the computer to be stored as List Mode Format (LMF) data.

As shown in Fig. 4, individual CsI(Na) pixels can be identified in the uniformity map and in the line profile. In addition, the

electronic readout provides low background noise and clear pixels identification, as it can be observed in both image and profile (Fig. 4). An average peak-to-valley ratio (P/V) of ~ 1.95 was calculated in the line profiles. Note that the reported P/V is calculated with no correction on the raw image nor the line profile.

2.1.3. Calibration

Calibrations of SURGEOSIGHT-I system were performed using a flood-filled phantom ($50 \times 50 \times 5 \text{ mm}^3$) with a uniform solution of 37 MBq activity of Tc-99m. The collimator of the system is installed in all of the calibrations.

In order to correct for the spatial distortions of the raw image, an in-house linearity calibration technique was used which is based on measurements using flood-field source with the collimator attached to the detector. First, for linearity calibration, a look-up table (LUT) was calculated from a 2-dimensional (2D) scan. For LUT calculation, a semi-automated peak detection

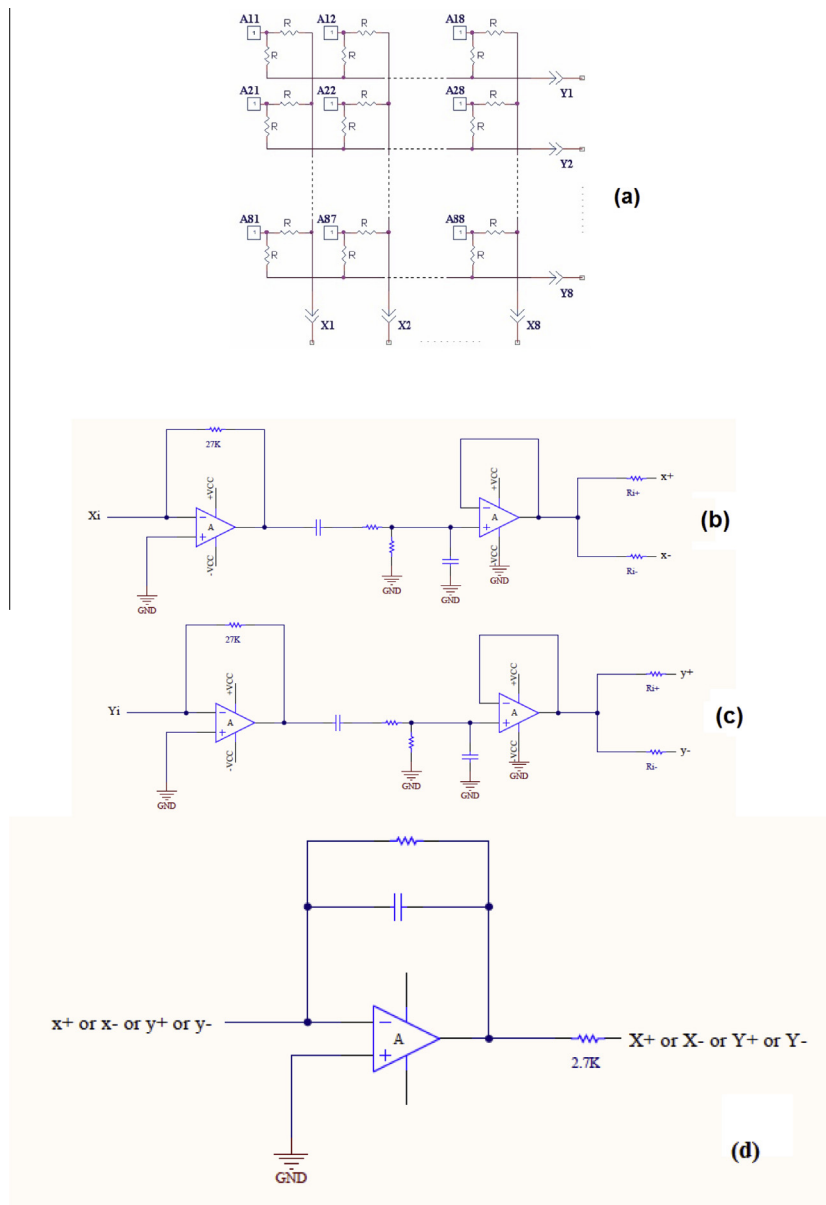


Fig. 3. Simplified circuit schematic of the resistive network board (a), Simplified circuit schematic of the pre-amplifier board for X and Y position signals. The printed circuit boards (PCBs) of them have been placed inside the head, (b) and (c). Simplified circuit schematic of the main board. In this board signal is amplified and then digitized using high-speed ADCs (d).

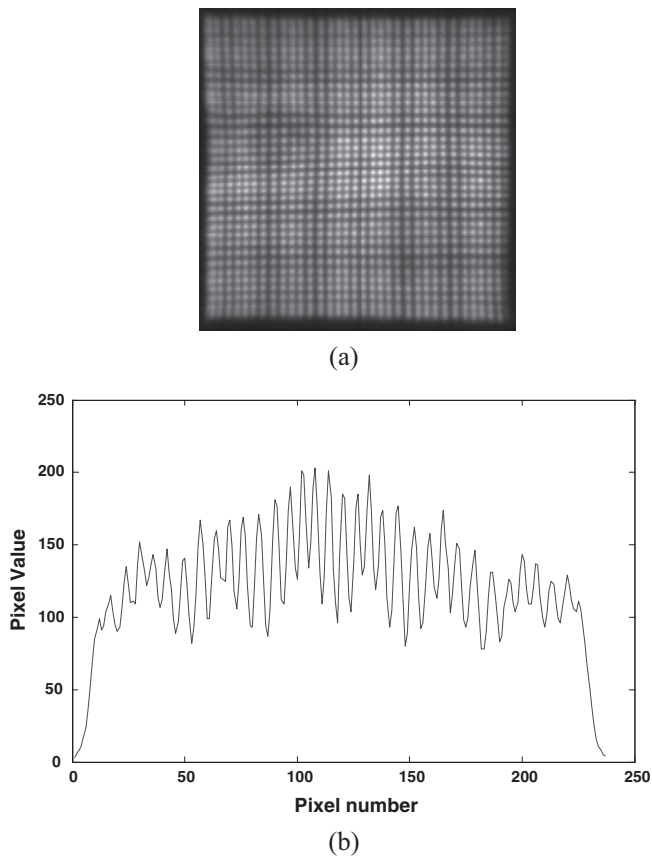


Fig. 4. Raw image (a) and horizontal profile (b) acquired with the uniform source of Tc-99m. The image referred to as a flood (or crystal) map. Each point in the image represents a crystal element. The average peak to valley ratio is ~ 1.95 .

algorithm determined the locations of the crystal peaks. Then, lines were drawn in the valleys between crystal peaks using a fully automated algorithm. The lines defined the crystal boundaries which were used by subsequent LUTs to identify the individual crystals. This LUT contains information about how to distribute the contents of each detector pixel (channel) onto the pixels of the final image.

The flood image was also used to calculate a spatially dependent energy discrimination table containing information about the position and the width of all photopeaks. Energy LUT was determined with an automated algorithm which finds the photopeak channel in each spectrum. During imaging, this LUT is used to calculate the energy correction factor for each crystal element.

This image may also be used for uniformity correction if it contains enough counts per pixel to reduce the pixel counts standard deviation below 1%. The correction factor for each pixel is defined as the mean pixel value divided by the individual pixel value.

2.2. Measurement of performance parameters of system

As mentioned earlier, performance parameters were measured using NEMA NU1-2007 protocol [20] throughout the paper, except if stated otherwise.

2.2.1. Intrinsic count rate performance

While count rate performance is usually evaluated using the decay method [20], we used a less time consuming technique similar to the one suggested by Geldenhuys, et al. [22]. This technique is based on using photon attenuator to modulate the incident

photon fluency for simulating radioactive decay to evaluate the count rate performance.

As shown in Fig. 5, a vial containing 185 MBq activity of Tc-99m solution was placed at a 35 cm distance from the detector surface without the collimator to irradiate the entire active area of the detector. Based on the NEMA standard if the source is placed at a distance at least five times greater than the largest linear dimension of the UFOV above the detector, it can be assumed that a uniform flux of radiation from the source is emitted toward the detector. In this study, 1 mm thick copper sheets were placed between the source and the detector to attenuate the count rate. Thereafter, a series of planar images were acquired for 60 sec with changing the total copper thickness each time. For each image, the total counts were calculated and corrected for decay, and then the measured count rate was calculated as the corrected total counts divided by the acquisition time. In order to determine the count rate curves, the logarithm of the observed count rate (OCR) versus the thickness of the copper plates was plotted. A line fitted to the low count rate region of the data was back-extrapolated to provide a value for no loss at higher count rates. So, true count rate (TCR) could be determined by fitting a line to low count rates in the aforementioned curve.

2.2.2. Energy resolution

The energy resolution was measured using a phantom ($50 \times 50 \times 5 \text{ mm}^3$) filled with a uniform solution of Tc-99m (18.5 MBq). According to NEMA protocols for pixelated detectors, the collimator was installed during data acquisition. A Gaussian fitting was applied to the data of the energy spectrum and the FWHM divided by the reference energy (here 140 keV) was reported as the energy resolution of the system.

2.2.3. Spatial resolution

The spatial resolution was characterized for different distances from the collimator using a capillary source (1.1 mm internal diameter) filled with 18 MBq Tc-99m solution. For each distance, the line source was scanned via several separate steps of 1 mm in the UFOV of the detector while the collimator was attached. All possible count profiles of the resulting line-spread functions (LSFs) in each step were then considered for Gaussian fitting

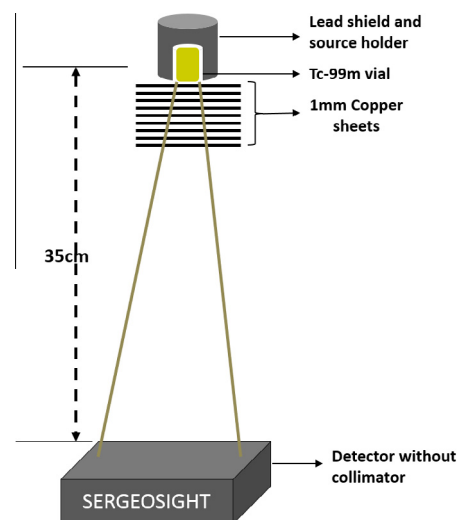


Fig. 5. Setup of the count rate performance measurement. The Tc-99m vial was placed in a lead shield at 35 cm distance from the collimator surface. 1 mm thick copper sheets were placed in front of the Tc-99m source as an attenuator to simulate different count rates.

(Eq. (1)) and FWHM calculation (Eq. (2)). The average of the FWHM values was reported as the FWHM for the corresponding distance from the collimator. The spatial resolution was measured on the collimator surface, 3 cm, 6 cm, and 10 cm from the collimator surface.

$$f(x) = a \times \exp \left[-\frac{(x - b)^2}{2\sigma^2} \right] \tag{1}$$

$$\text{FWHM} \approx 2.35\sigma \tag{2}$$

where a , b , and σ are the height of the curve peak, the mean, and the standard deviation, respectively.

2.2.4. System uniformity

The system uniformity was obtained with the same flood-field source used in Section 2.2.2. The phantom was placed in direct contact with the collimator. The integral and the differential uniformity values were calculated in the UFOV and the central field-of-view (CFOV), ignoring the marginal pixels and smoothing the image with a 3×3 kernel filter, according to NEMA NU1-2007 [20].

2.2.5. Noise characteristics

To investigate the noise characteristic of the detector, the same flood-field source used in Section 2.2.2 was positioned on top of the detector while the collimator was mounted. Flood image was acquired with mean of 200 counts/pixel. Standard deviation as a measure of noise was calculated for the UFOV.

2.2.6. System sensitivity

The sensitivity was measured using a cylindrical phantom with an inner diameter of 32 mm filled with 18.5 MBq activity of Tc-99m. The sensitivity variations were determined as a function of distance; the phantom was placed at 0 cm, 5 cm, and 10 cm distance from the collimator surface.

2.2.7. Shielding leakage

The shielding leakage is defined as the penetration of the photons into the shielding. This value was measured with a vial containing 37 MBq activity of Tc-99m solution inserted within a lead container with a single hole. Shielding leakage is calculated as the ratio of the maximum count rate when the source was moved at a 10 cm distance from the side of the detector to the count rate

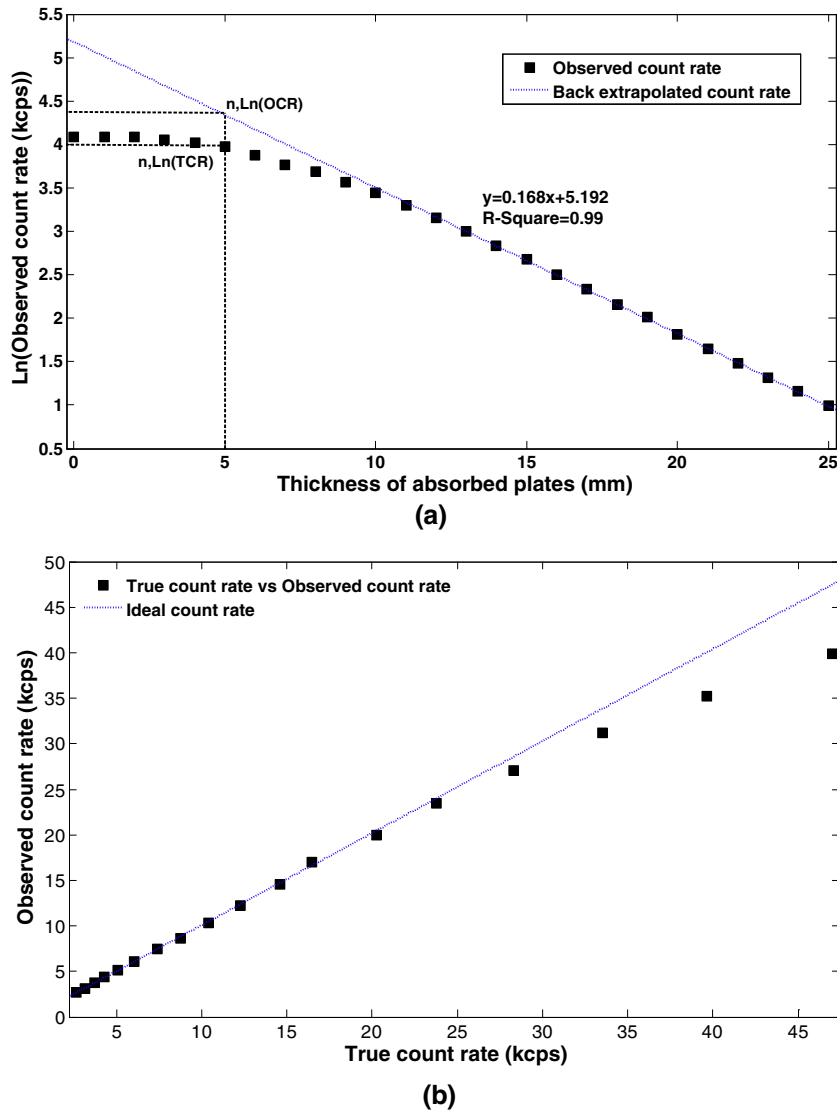


Fig. 6. Observed count rate from a Tc-99m point source against the thickness of the copper plates. A line fitted to data in low count rate region for determination of true count rate (a), Observed count rate as a function of true count rate (b).

when the source is placed 10 cm in front of the collimator surface. The source should be moved around the sides and also the back of the detector to find the location of the maximum count rate. The percent shielding leakage was calculated by the following equation [20]:

$$\text{Shield Leakage(\%)} = \frac{\text{Max Shield CountRate}}{\text{Collimator CountRate}} \times 100 \quad (3)$$

3. Results

Fig. 6(a) illustrates the graph of the logarithm of the OCR against the thickness of the absorber plates. A line was fitted to the linear region of the data. The curve demonstrates the deviation of the observed count rate points from the true incident count rate as a result of the scintillation camera dead-time. Values of OCR and TCR were determined from the curve shown in Fig. 6(a) and plotted in Fig. 6(b) as count rate curves. The observed count rate for a 20% count loss is approximately 41.6 kcps.

The average extrinsic energy resolution was measured about 50% and 20.6% before and after energy correction, respectively. Energy spectrum of SURGEOSIGHT-I after energy correction is demonstrated in Fig. 7.

Fig. 8(a) shows the planar image of the capillary source located on the collimator surface and the count profile (representing the LSF) in addition to the Gaussian curve fitted to data, respectively (Fig. 8(b)). As shown in Fig. 9 the resolution is ~2.2 mm FWHM on the surface of the collimator and 9.4 mm FWHM at 10 cm from the collimator. The results demonstrate that spatial resolution has a linear trend with distance.

The integral and differential uniformity values are calculated based on the flood-filled images before (Fig. 10(a)) and after uniformity correction (Fig. 10(b)). The images show the improvement of the image uniformity after uniformity correction. The uniformity parameters of the system were summarized in Table 1. The results illustrate the improvement of image uniformity after correction in the system.

The standard deviation of flood image was 0.3.

The system sensitivity on the collimator surface, 5 cm, and 10 cm distant from the collimator is 142 cps/MBq, 134 cps/MBq, and 81 cps/MBq, respectively.

The detector shielding leakage was calculated 2%. Maximum shield leakage was measured on the backside of the detector.

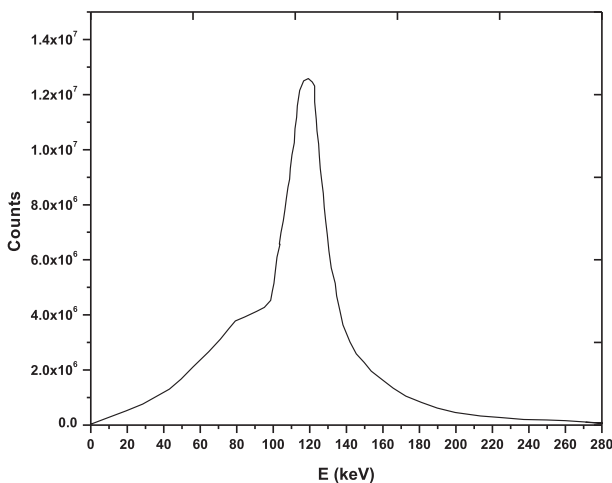


Fig. 7. The Tc-99m energy spectrum of SURGEOSIGHT-I. All the UFOV events have been considered in the spectrum.

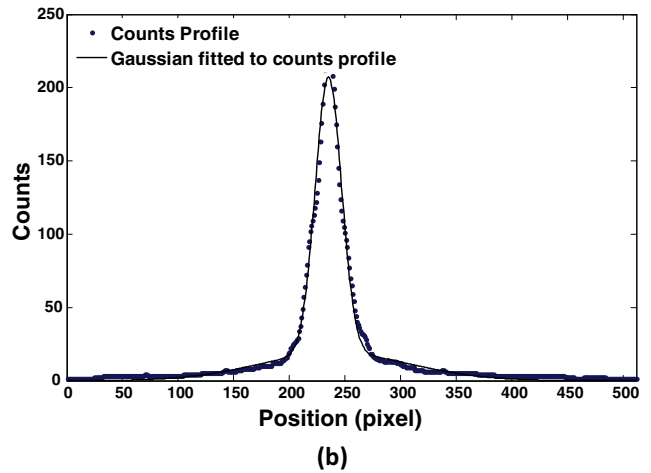
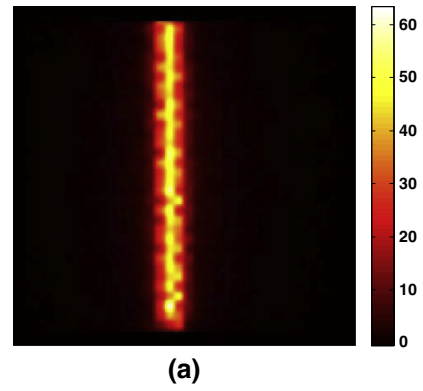


Fig. 8. The image of a capillary source placed on the collimator surface (a), together with its corresponding count profile (representing the LSF) and the Gaussian curve fitted on it (b).

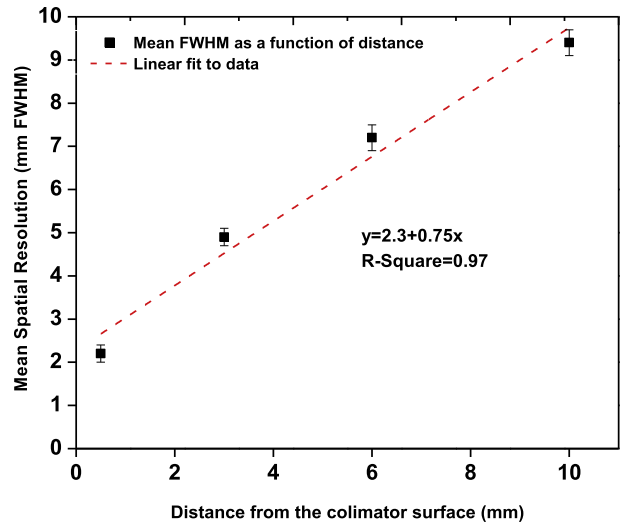


Fig. 9. Spatial resolution as a function of distance from the collimator surface.

4. Discussion and conclusion

The SURGEOSIGHT-I is a new mini gamma camera specifically designed for pre-operative and intra-operative scintigraphy. This study evaluated the performance of SURGEOSIGHT-I in order to assess its capabilities for identifying SLNs. The evaluation was mainly based on the NEMA NU1-2007 protocol [20] for investigating the performance of systems with pixelated crystal.

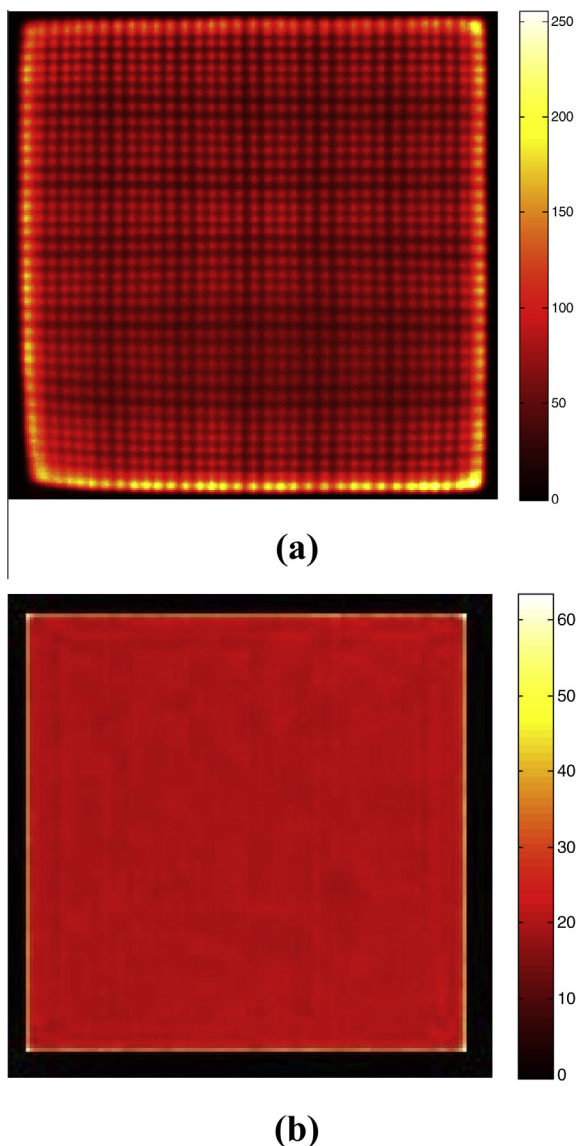


Fig. 10. The images of the uniformity phantom with (a) and without (b) uniformity correction.

Table 1
Uniformity analysis before and after uniformity correction.

	Without Uniformity correction		With Uniformity correction	
	UFOV	CFOV	UFOV	CFOV
Integral Uniformity (%)	55.4	54	4.5	4.5
Differential Uniformity (%)	42.1	29.6	7.7	4.6

The results showed that the count rate response of the system has a linear trend up to 31 kcps. The detector shows a linear behavior at activities below 890 MBq showing the sensitivity of 142 cps/MBq. However, it should be noted that the typical activities used in the breast cancer studies are maximum 37 MBq [13,15,23].

The average extrinsic energy resolution was measured about 50% and 20.6% before and after energy correction, respectively. It is well known that the energy resolution of pixelated detectors is a function of both pixel size and also intrinsic efficiency of the crystal material [24]. The total energy spectrum is affected by the

non-uniform response of the PSPMTs, as well as the loss of signal in the area between the pixels of the crystal. However, by calculating the energy spectrum of each crystal cell and by normalizing them using the peak shift method, an improved total normalized energy spectrum was obtained [24,25]. So this configuration of small gamma cameras often has a FWHM energy resolution that is poorer than single crystal scintillation cameras [26–29]. However, we believe that the scintillator array we used in this work has a relatively poor energy resolution. Therefore, with uniform crystal with larger light yield, we can achieve more light collection efficiency at the photodetector plane leading to an improved energy resolution.

The measurement of the LSF with a static line source is appropriate for small gamma cameras having LSFs that approximate to a Gaussian. The LSF was measured by aligning the line source along one axis of the detector and moving it perpendicular to its length in 1 mm steps. The mean resolution on the collimator surface was ~ 2.2 mm FWHM increasing to 9.4 mm FWHM at the distance of 10 cm from the collimator surface.

The system sensitivity was measured as 142 cps/MBq on the collimator surface and 134 cps/MBq, in 10 cm distance from the collimator surface. As expected for parallel-hole collimation, a small decrease is observed when distance is increased [30,31]. The sensitivity decreased sharply when the distance exceeds the size of detector FOV.

The system integral uniformity after uniformity correction was obtained 4.5% in both of the UFOV and the CFOV. The differential uniformity after uniformity correction was calculated 4.6% and 7.7% for the UFOV and CFOV, respectively. The uniformity values are compared with those reported in the literature for small-FOV gamma cameras [11,32,33].

The detector shielding leakage was about 2%. The shield leakage for the portable gamma cameras is important because such systems should be used in close contact with the patient's body, thus the out-of-FOV radioactivity may be very close to the side or back shielding of the detector causing image distortion.

An appropriate gamma camera for intra-operative use is the one with high sensitivity, enough shielding, high spatial resolution and easy handling of system with articulated arm and low weight of head. However, no gamma camera can have optimal values for all of the mentioned parameters; for instance, there is an intrinsic compromise between sensitivity and spatial resolution using the parallel hole collimator. Therefore, it is reasonable to assume that the best gamma camera is the one having the best compromise of the performance parameters for the specific application. In this view, the best trade-off strictly depends on the type of study that is planned. For example, when the predominant use of the gamma camera is SLN biopsy in patients with breast cancer or with melanoma, the most important parameter for target detection is sensitivity [34,35]. In fact, it is crucial for the gamma camera to be able to detect lymph nodes with low uptake. On the other hand, maximum spatial resolution, although desirable, is relatively less important than sensitivity for SLN procedures, especially in surgical protocols including complete removal of all hot sentinel nodes.

The NEMA protocols provide a standard platform for comparing various gamma cameras regarding their performance parameters [36]. Table 2 compares the main features of our gamma camera with other small gamma cameras reported in the literature or used as commercial systems. As shown, CrystalCam gamma camera reported by Knoll et al. [19] with semiconductor CZT detector provide better energy resolution. However, Sentinella 102 that used pinhole collimator can achieve higher sensitivity while the its resolution is poorer than the other systems. The SURGEOSIGHT-I has a comparable image quality with other gamma cameras that utilize parallel-hole collimator.

Table 2
NEMA performance parameters of the SURGEOSIGHT-I in comparison to some available gamma cameras.

Manufacturer and type	Detector type	Sensitivity (cps/MBq)	Spatial resolution FWHM (mm)	Energy resolution (%)
SURGEOSIGHT-I (this study)	pixelated CsI(Na), PSPMT, LEGP ^a collimator	142	2.2	20.6
Trotta et al. [16]	pixelated CsI(Na), PSPMT, square parallel-hole collimator	204	2.5	N/A
Olcott et al. [13]	pixelated NaI(Tl), PSPMT, LEHS ^b collimator	135	1.6	12.3 (intrinsic)
Goertzen et al. [37]	CsI(Tl), SiPM ^c , LEHR ^d collimator	149.7	3.46	38.9
CrystalCam camera Knoll et al. [19]	CZT, LEHR collimator	237	1.93	5.2
POCI, Menard et al. [38]	YAP, position sensitive diode, LEHR collimator	200	1.9	38
Sentinella 102, Sanchez et al. [39]	continuous CsI(Na), PSPMT, 4 mm pinhole collimator	90–900 at source to aperture distance: 1–10 cm	10–18 at source to aperture distance: 3–10 cm	15.9

^a Low-energy general-purpose.

^b Low-energy high-sensitivity.

^c Silicon Photomultiplier.

^d Low-energy high-resolution.

While the results of our first prototype system are encouraging, we will continue to improve the overall system performance for the next generation of the SURGEOSIGHT-I platform. This includes further enhancement of the energy resolution as well as other key performance metrics such as spatial resolution, image contrast, and system sensitivity mainly by using higher light yield crystals for better energy resolution. System performance is also capable to be improved with pinhole collimator. The presented system can be used for a number of clinical applications including sentinel node detection and radiopharmaceutical-guided surgery. Future work will include various phantom and clinical studies.

Acknowledgments

This work was supported under Grant number 20386, Tehran University of Medical Sciences, Tehran, Iran.

References

- [1] Morton DL, Wanek L, Nizze JA, Elashoff RM, Wong J. Improved long-term survival after lymphadenectomy of melanoma metastatic to regional nodes. Analysis of prognostic factors in 1134 patients from the John Wayne Cancer Clinic. *Ann Surg* 1991;214:491.
- [2] Wunderbaldinger P, Josephson L, Bremer C, Moore A, Weissleder R. Detection of lymph node metastases by contrast-enhanced MRI in an experimental model. *Magn Reson Med* 2002;47:292–7.
- [3] Morton DL, Ollila DW. Critical review of the sentinel node hypothesis. *Surgery* 1999;126:815–9.
- [4] Wawroschek F, Vogt H, Weckermann D, Wagner T, Harzmann R. The sentinel lymph node concept in prostate cancer—first results of gamma probe-guided sentinel lymph node identification. *Eur Urol* 1999;36:595–600.
- [5] Britten AJ. A method to evaluate intra-operative gamma probes for sentinel lymph node localisation. *Eur J Nucl Med* 1999;26:76–83.
- [6] Jakub JW, Pendas S, Reintgen DS. Current Status of sentinel lymph node mapping and biopsy: facts and controversies. *Oncologist* 2003;8:59–68.
- [7] Tanis PJ, Nieweg OE, Olmos RAV, Emiel J, Kroon BB. History of sentinel node and validation of the technique. *Breast Cancer Res* 2001;3:109.
- [8] Bricou A, Duval MA, Charon Y, Barranger E. Mobile gamma cameras in breast cancer care – a review. *Eur J Surg Oncol (EJSO)* 2013;39:409–16.
- [9] Cardona-Arboniés J, Mucientes-Rasilla J, Moreno Elola-Olaso A, Salazar-Andía G, Prieto-Soriano A, Chicharro de Freitas J, et al. Contribution of the portable gamma camera to detect the sentinel node in breast cancer during surgery. *Rev Esp Med Nucl Imagen Molecular* 2012;31:130–4 [English Edition].
- [10] Rietbergen DDD, van den Berg NS, van Leeuwen FWB, Valdés Olmos RA. Hybrid techniques for intraoperative sentinel lymph node imaging: early experiences and future prospects. *Imaging Med* 2013;5:147–59.
- [11] Ferretti A, Chondrogiannis S, Marcolongo A, Rubello D. Phantom study of a new hand-held c-imaging probe for radio-guided surgery. *Nucl Med Commun* 2013;34:86–90.
- [12] Bugby SL, Lees JE, Bhatia BS, Perkins AC. Characterisation of a high resolution small field of view portable gamma camera. *Physica Med* 2014;30:331–9.
- [13] Olcott P, Praxt G, Johnson D, Mitra E, Niederkohr R, Levin CS. Clinical evaluation of a novel intraoperative handheld gamma camera for sentinel lymph node biopsy. *Physica Med* 2014;30:340–5.
- [14] Heller S, Zanzonico P. Nuclear probes and intraoperative gamma cameras. *Semin Nucl Med* 2011;41:166–81.
- [15] Tsuchimochi M, Hayama K. Intraoperative gamma cameras for radioguided surgery: technical characteristics, performance parameters, and clinical applications. *Physica Med* 2013;29:126–38.
- [16] Trotta C, Massari R, Palermo N, Scopinaro F, Soluri A. New high spatial resolution portable camera in medical imaging. *Nucl Instrum Methods Phys Res Sect A* 2007;577:604–10.
- [17] Fernández M, Benlloch J, Cerdá J, Escat B, Giménez E, Giménez M, et al. A flat-panel-based mini gamma camera for lymph nodes studies. *Nucl Instrum Methods Phys Res Sect A* 2004;527:92–6.
- [18] Sanchez F, Benlloch J, Escat B, Pavón N, Porras E, Kadi-Hanifi D, et al. Design and tests of a portable mini gamma camera. *Med Phys* 2004;31:1384–97.
- [19] Knoll P, Mirzaei S, Schwenkenbecher K, Barthel T. Performance evaluation of a solid-state detector based handheld gamma camera system. *Front Biomed Technol* 2014;1:61–7.
- [20] Section NEMAN. Performance measurements of scintillation cameras. National Electrical Manufacturers Association; 2007.
- [21] Anger HO. Scintillation camera. *Rev Sci Instrum* 1958;29:27–33.
- [22] Geldenhuys EM, Lötter MG, Minnaar PC. A new approach to NEMA scintillation camera count rate curve determination. *J Nucl Med* 1988;29:538–41.
- [23] Thompson M, Korourian S, Henry-Tillman R, Adkins L, Mumford S, Smith M, et al. Intraoperative radioisotope injection for sentinel lymph node biopsy. *Ann Surg Oncol* 2008;15:3216–21.
- [24] Zaidi H. Quantitative analysis in nuclear medicine imaging. US: Springer; 2006.
- [25] Rasouli M, Takavar A, Ay MR, Saber S, Loudos G. Effects of crystal pixel size and collimator geometry on the performance of a pixelated crystal γ -camera using Monte Carlo simulation. *J Nucl Med Technol* 2010;38:199–204.
- [26] Levin C, Hoffman E, Tomai M, MacDonald L. PSPMT and photodiode designs of a small scintillation camera for imaging malignant breast tumors. *IEEE Trans Nucl Sci* 1997;44:1513–20.
- [27] David S, Georgiou M, Fysikopoulos E, Belcari N, Loudos G. Imaging performance of silicon photomultipliers coupled to BGO and CsI: Na arrays. *J Instrum* 2013;8:P12008.
- [28] Deprez K, Van Holen R, Vandenberghe S. A high resolution SPECT detector based on thin continuous LYSO. *Phys Med Biol* 2014;59:153.
- [29] Bouckaert C, Marcinkowski R, Deprez K, Espana Palomares S, Van Holen R, Vandenberghe S. Optimization of digital silicon photomultipliers for monolithic SPECT scintillators. *J Nucl Med* 2012;2160.
- [30] Sajedi S, Zeraatkar N, Moji V, Farahani MH, Sarkar S, Arabi H, et al. Design and development of a high resolution animal SPECT scanner dedicated for rat and mouse imaging. *Nucl Instrum Methods Phys Res Sect A* 2014;741:169–76.
- [31] Moji V, Zeraatkar N, Farahani MH, Aghamiri MR, Sajedi S, Teimourian B, et al. Performance evaluation of a newly developed high-resolution, dual-head animal SPECT system based on the NEMA NU1-2007 standard. *J Appl Clin Med Phys* 2014;15.
- [32] Jeong MH, Choi Y, Chung YH, Song TY, Jung JH, Hong KJ, et al. Performance improvement of small gamma camera using NaI (TI) plate and position sensitive photo-multiplier tubes. *Phys Med Biol* 2004;49:4961.
- [33] Jeong MH, Choi Y, Chung YH, Song TY, Jung JH, Hong KJ, et al. Position mapping, energy calibration, and flood correction improve the performances of small gamma camera using PSPMT, Nuclear Science Symposium Conference Record. Portland, Oregon, USA: IEEE; 2003. pp. 2103–2107.
- [34] Mariani G, Gipponi M, Moresco L, Villa G, Bartolomei M, Mazzarol G, et al. Radioguided sentinel lymph node biopsy in malignant cutaneous melanoma. *J Nucl Med* 2002;43:811–27.
- [35] Riccardi L, Gabusi M, Bignotto M, Gregianin M, Vecchiato A, Paiusco M. Assessing good operating conditions for intraoperative imaging of melanoma sentinel nodes by a portable gamma camera. *Physica Med* 2015;31:92–7.

- [36] Bhatia BS, Bugby SL, Lees JE, Perkins AC. A scheme for assessing the performance characteristics of small field-of-view gamma cameras. *Physica Med* 2015;31:98–103.
- [37] Goertzen AL, Thiessen JD, McIntosh B, Simpson MJ, Schellenberg J. Characterization of a handheld gamma camera for intraoperative use for sentinel lymph node biopsy, IEEE Nuclear Science Symposium and Medical Imaging Conference. Korea, Seoul: IEEE; 2013. pp. 1–4.
- [38] Menard L, Charon Y, Solal M, Laniece P, Mastrippolito R, Pinot L, et al. POCl: a compact high resolution γ camera for intra-operative surgical use. *IEEE Trans Nucl Sci* 1998;45:1293–7.
- [39] Sánchez F, Fernández M, Giménez M, Benlloch J, Rodríguez-Alvarez M, De Quirós FG, et al. Performance tests of two portable mini gamma cameras for medical applications. *Med Phys* 2006;33:4210–20.